Electronic Supplementary Material (ESI) for Chemical Communications.
This journal is © The Royal Society of Chemistry 2022

Supplementary Information

Experimental Procedures

1.0 Peptide Synthesis- Short peptide amphiphiles (sPA1 and sPA2) were synthesized by conventional solution-phase synthesis via our standard lab protocol.[30] the detailed synthesis method and characterization are already reported in the paper(K. B. Joshi et al. *Chem.: Asian J.*, **2020**, 15(4), 531-539). The compound used in this study was from the same batch and therefore directly used.

2.0 UV studies- A 200 µM solution of each **sPA1**&**2** in ethanol with 1 mM aqueous solution of $HAuCl_4$ was mixed in two separate glass vials and then kept in sunlight for the required time. UV-Vis spectra were recorded in 1 min time interval for $HAuCl_4$ mixed sPA1 & 2 solutions up to the saturation of SPR band or up to the full reduction of metal ion i.e. Au(III) to Au(0) by LAB INDIA UV 3092 spectrophotometer with 10 mm quartz cell at 25±0.1 °C

3.0 Transmission Electron Microscopy (TEM)-Freshly prepared 2 µL aliquots of every test sample were transferred to 400 mesh carbon-coated copper grids and dried at room temperature for 30 minutes, followed by vacuum drying. The samples were analyzed with the FEI Technai 20 U Twin Transmission Electron Microscope.

4.0 MATLAB Analysis-The background of the image was estimated using the morphological operation function. This estimated background has been subtracted from the main image. The image contrast was improved, and then the grayscale image was changed to a binary image for further processing. The "graythresh" function was used to compute an appropriate threshold to use to convert the grayscale image to binary. Also, background noise was removed with"bwareaopen" function and the processed image was preserved.

5.0 FT-IR Study- FT-IR spectra were recorded on a Bruker Alfa II ATR. The FT-IR spectra for sPAs and sPAs-Au(III) and AuNPs were carried out for the functional group and secondary structural analysis. Spectra were recorded in the spectral range of 4000–500 cm^{-1} at 4 cm^{-1} spectral resolution, 2 sample gain, and 32 sample/background scans using OPUS 7.0 computer software and removed unwanted noise. A small aliquot (5 µl)of 200 µM solution of **sPA1**&**2** alone and with Au(III) and AuNPs were deposited over the ZnSe plate and dried. The secondary structural contribution was calculated by Deconvolution of amide band at 1700-1600 cm^{-1} by multiple Gaussian peaks fitting using origin software. The numbers of initial peak values were taken from the second derivative spectrum.

6.0 Atomic Force Microscopy (AFM). All the test samples were placed on freshly cleaved muscovite mica surfaces followed by imaging with an atomic force microscope (INNOVA, ICON analytical equipment, Bruker, operating under the acoustic AC mode (AAC or tapping mode), with the aid of a cantilever [NSC 12(c) from MikroMasch, Silicon Nitride Tip] by NanoDrive™ version 8 software. The force constant was ~2.0 N/m, while the resonant frequency was ~280 kHz. The images were taken in air at room temperature, with the scan speed of 1.5 lines/sec. The data analysis was done using nanoscope analysis software. The sample-coated substrates were dried at dust free space for 30 min followed by high vacuum drying and subsequently examined under AFM.

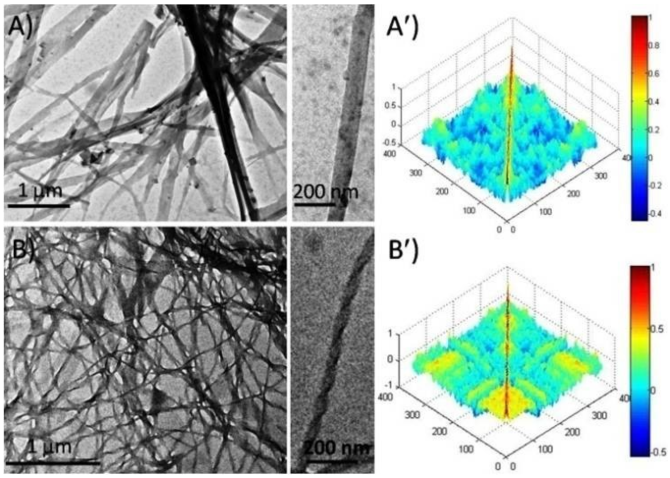

Figure S1. Depicts A) self-assembled structures of 200 µM solution of **sPA1** and inset shows: single and intact, robust and straight fiber, A’) corresponding covariance matrix plot (A’) obtained by Matlab program-processed image (A). Image B) depicts self-assembled structures of 200 µM solution of **sPA2** and inset shows: **a** single twisted or helical fiber B’) corresponding covariance matrix plot.

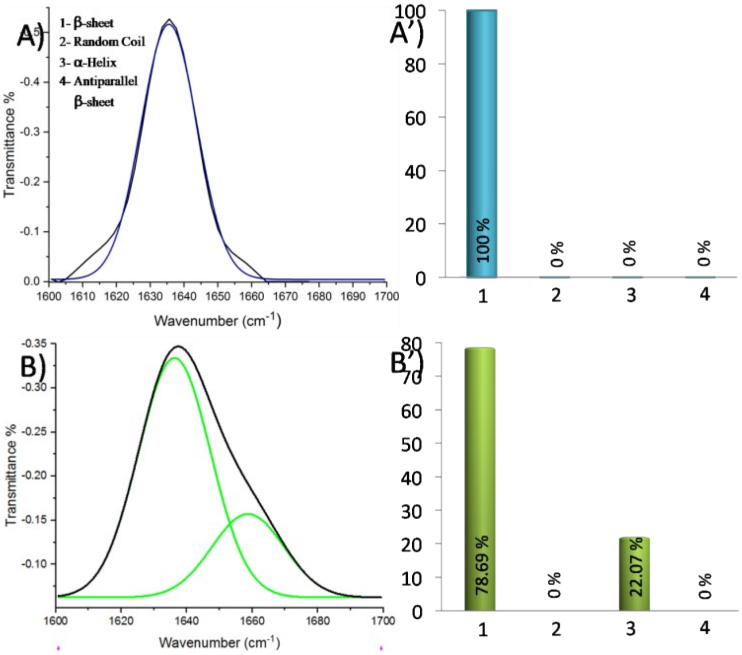

Figure S2. The picture depicts a deconvolution analysis of the amide I region (1600-1700 cm^{-1}) of 200 µM sPA1 and sPA2 solution. A) FT-IR spectra of 200 µM solution of **sPA1** and A’) represent the corresponding distribution of secondary structural components. B) FT-IR spectra of 200 µM solution of sPA2 and B’) represent the corresponding distribution of secondary structural components.

7.0 Model Discription-Formation of Sheets and Helices: A proposed model for the formation of sheets and helices (Figure S3) discribed that the formation of two different structures. These observations are further supported by the results obtained from FT-IR spectroscopy and Transmission electron microscopy. The different nature of self-assembly is primarily depends upon the sequence peptide amphiphile in which sPA1 contain **Pal-Phe-Tyr-β-Ala-OH** whereas sPA2 contain **Pal-Tyr-Phe -β-Ala-OH.** The presence of Tyr residue in between two highly hydrophobic group in sPA2 perhaps directing the lateral (sidewise) interactions and therefore may lead to helical formation(Figure S3-B). However an ordered arrangement of hydrophobic (palmitoyl and phenylalanine) in sPA1 followed by hydrophilic (Tyr and β-Alanine) groups may favors direct interaction and lead straight and robust fibers hence sheets(Figure S3-A).

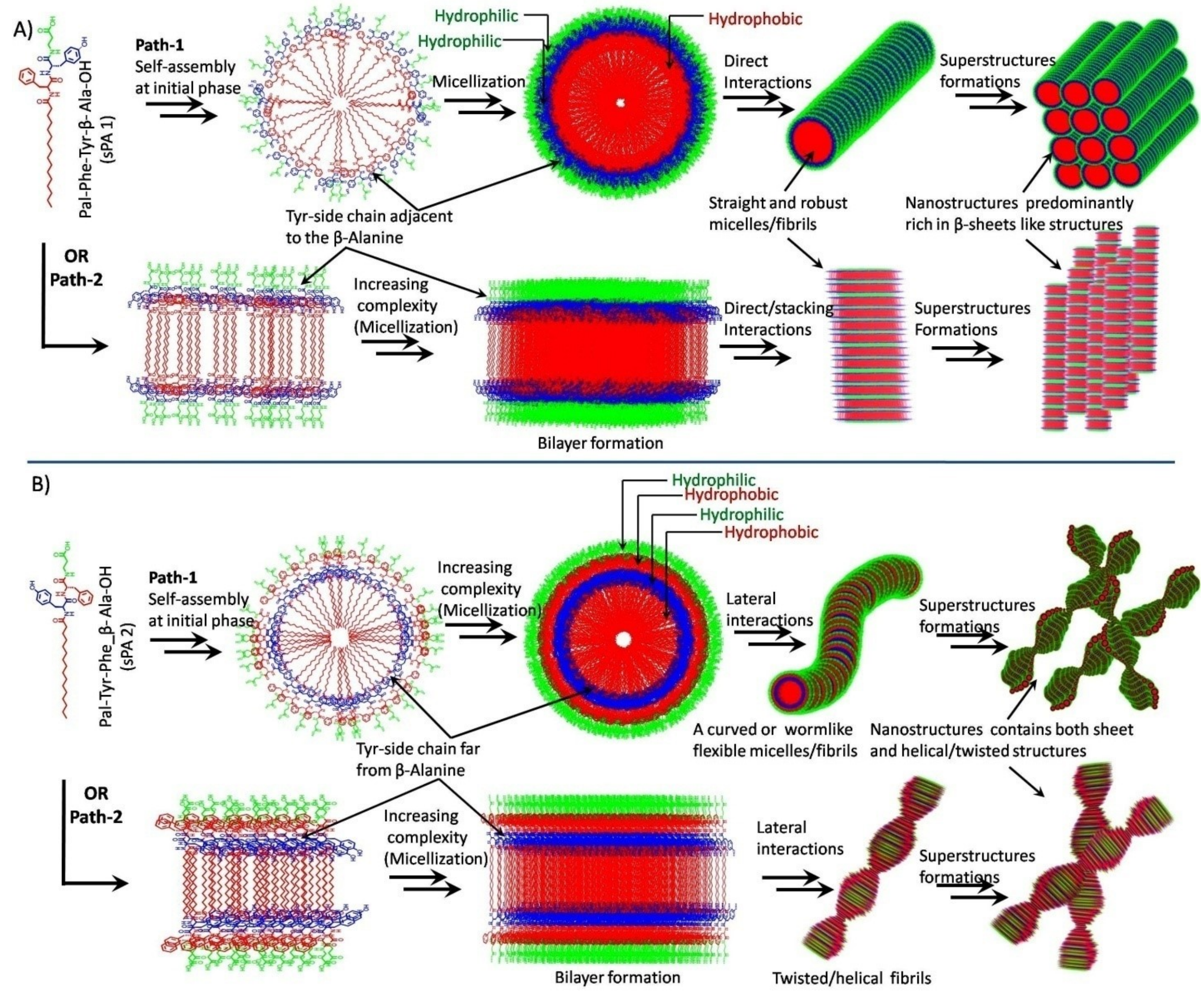

Figure S3: Depicts the proposed model for the formation of sheeted and helix structures by sPA1 and sPA2 respectively. A) Represent the formation of straight and robust fiber formation either via path1 or path 2, similarly B) the twisted or helical fiber formation can also be obtained either by path1 or path 2.

8.0 Preperation of Gold Nanoparticles and Characterizations: To prepare GNPs by using sPA1 and 2, a 200 µM solution of each sPA with 200 µM solution of Au(III) ions were incubated and the glass vials were kept in direct sunlight for 15 min. The yellow color of Au(III) ion mixed sPA solution turned into purple-red colour and UV-Vis spectra were recorded for both solutions (Fig.S4). Interestingly the SPR band for both the solution showed absorption maxima centred at 550 nm (Fig S4 and S5) thus revealed that both the conjugates perhaps providing almost similar kind of gold nanoparticles.[32] A time dependent UV-Vis spectra were recorded for both the solutions and the formation of GNPs were confirmed by the appearance of SPR band centred at absorption maxima (λ_{max}) 550 nm (Fig. S5). It is also observed that the formation of GNPs took little more time, 0-16 min for sPA1 however in the presence of sPA2 it took only 10 min (Fig.S5A & C inset).

9.0 Purification of AuNPs embadded nanobangles samples: Purification of GNPs-sPA colloid samples done by using centrifugation method before using it for the imaging/analysis. After the formation of GNPs-Peptide hybrids the solution was centrifuged at 12,000g for 15 minutes followed by removal of the supernatant and washing with ethanol. The residue was re-dissolved in the ethanol in the appropriate volume of solvent and used for further analysis.

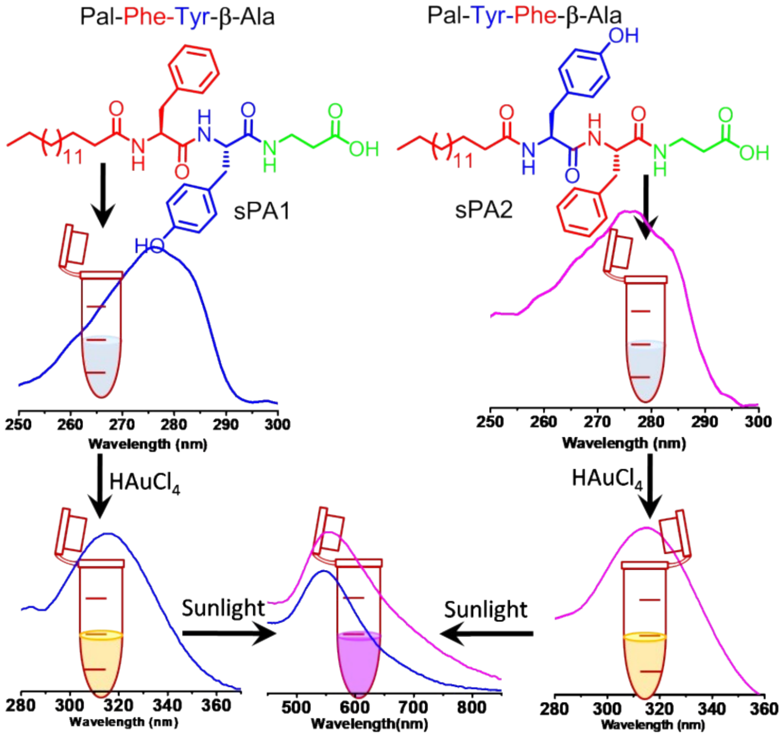

Figure S4. Depicts Top: the structure consists of lipidation of tripeptide conjugates using palmitic acid consist of hydophobic domain, aromatic core and a linear amino acid leading to a series of short peptide amphiphile (sPA) that is showing the shuffling of viz. two key amino acids (or a dipeptide unit) to give two different constitutional isomers namely **sPA1** & **sPA2**. Below: representing the process of formation of sPA-AuNPs hybrids. UV-Vis spectra of **sPA1** & **sPA2** for aromatic region, with Au(III) and at the centre: SPR band of AuNPs in the presence of **sPA1** & **sPA2** on a short exposure to sunlight.

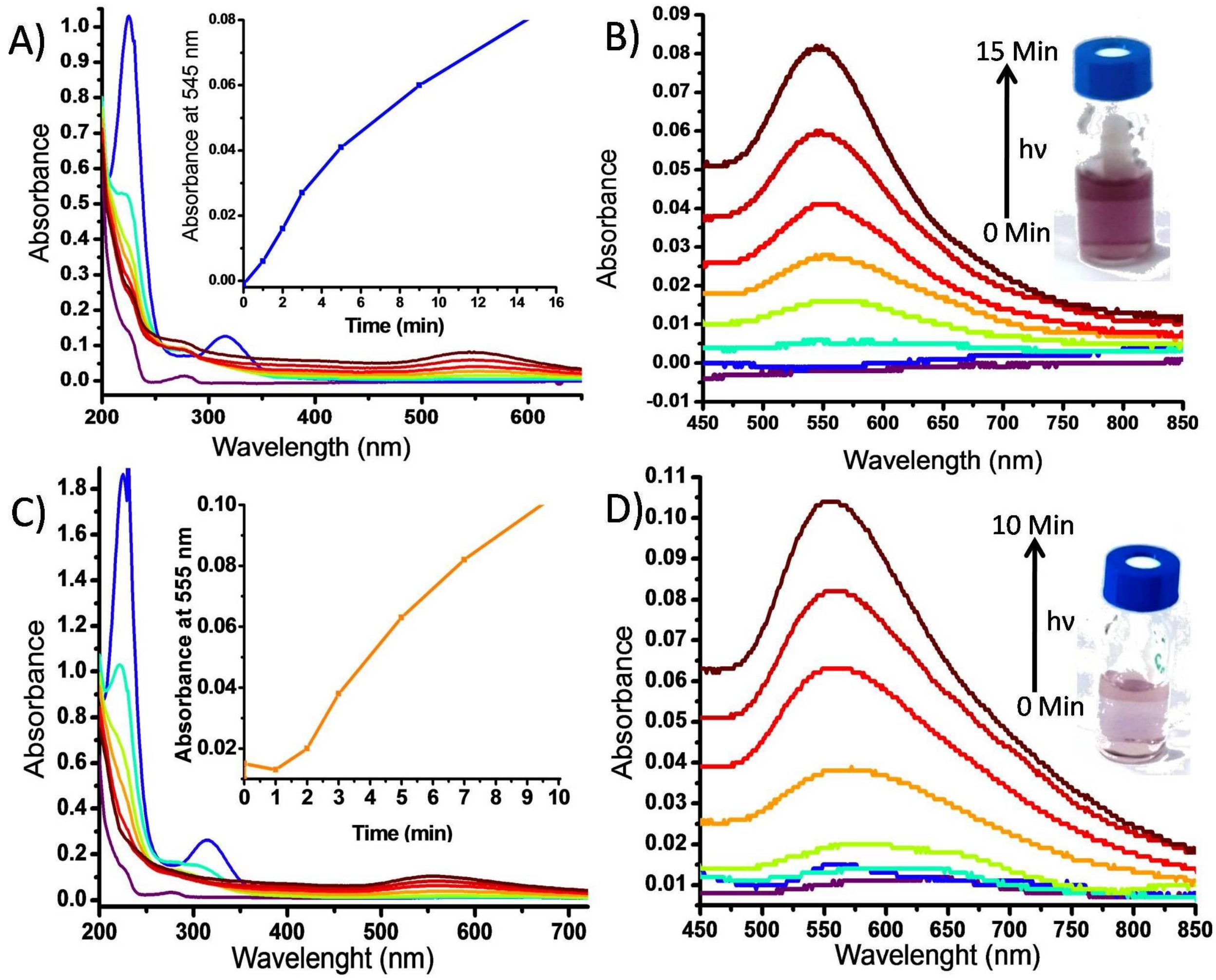

Figure S5: Time-dependent UV-Vis kinetics represent formation of GNPs-in 200 µM sPA1 & 2 solution in presence of sunlight; A & C) represents complete spectrum of a mixture of sPAs + Au(III) at different time intervals for sPA1 & 2 solution respectively; *inset:* represents the time taken by sPA1 &2 for GNPs formation by recording SPR band at 550 nm w.r.t. time. B&D) Nature of formed SPR band in the presence of sPA1 & 2 and inset: represents the color of GNPs-sPA solution. *Inset:* a sigmoidal curve fit.

10.0 FT-IR analysis of Au(III)/GNPs interaction with sPA: The amide I region (1600 to 1700 cm^{-1}) of **sPA1** and **2** were processed and deconvoluted. Interestingly, **sPA1** delineate the presence of β-sheet type secondary structures with 84.97%, which was 100% without Au(III) ions, along with emergence of random coil structures with 14.45% contribution (Fig. S6A vs Fig. S7A) while

sPA2 depicts decreased amount of β-sheet components from 78.69% (Fig.S6B′) to 51.99% (Fig. S7B′) along with increased helical content from 22.07% (Fig.S6B’) to 47.99% (Figure S7B’). The plausible reason for such change on secondary structural behavior is distinct amphipathic nature of shuffled amino acids in sPA, and presence of electrostatic interactions due to Au(III) ions. Consecutive order of amphipathicity (hydrophobic-hydrophobic-hydrophilic-hydrophilic) in **sPA1** resulted of β-sheets like structure along with some randomness while cumulative order of amphipathicity (hydrophobic - hydrophilic - hydrophobic - hydrophilic) resulted β-sheet like secondary structure along with presence helical content.

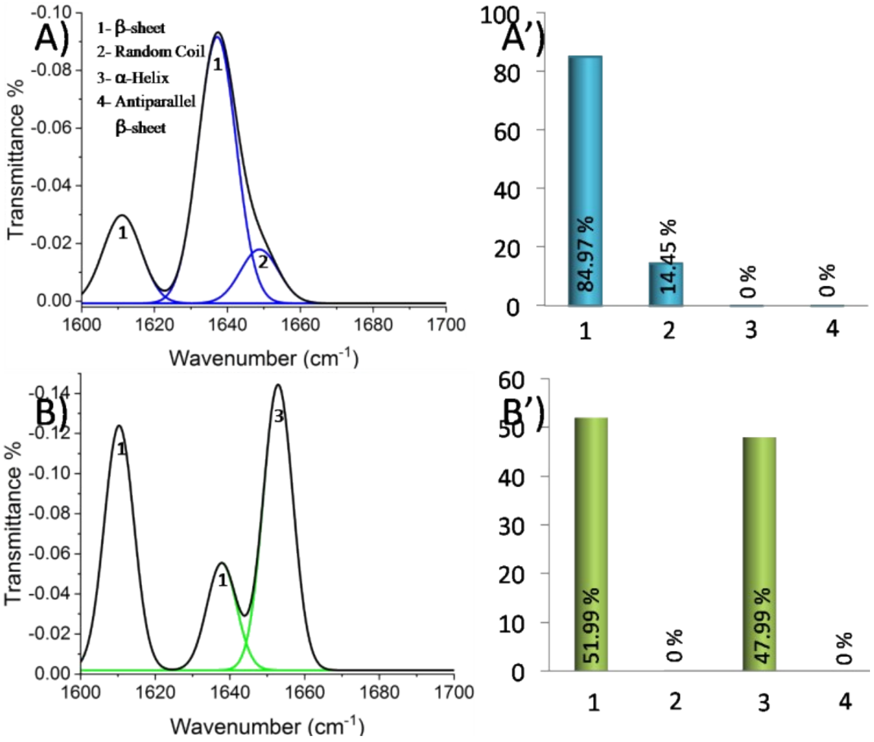

Figure S6. The picture depicts a deconvolution analysis of the amide I region (1600-1700 cm^{-1}) of 200 µM **sPA1** and **sAP2** with Au(III) ions solution. A) FT-IR spectra of solution of **sPA1-Au(III)** and A’) represent the corresponding distribution of secondary structural components. B) FT-IR spectra of solution of **sPA2- Au(III)** and B’) represent the corresponding distribution of secondary structural components.

FT-IR spectra of sPA-GNPs were also recorded and the amide I region (1600 to 1700 cm-1) was processed to check the secondary structural changes in the sPAs. The amide I band was deconvoluted followed by curve fitting. It is revealed that sPA1 exhibited 67.69 %, β–sheet, 24.17% of the random coil, and 7.90 % of anti-parallel β-sheet-like secondary structures (Figure S7A & A′) while sPA2 exhibited a mixed type of secondary structures that comprises 22.18 % β-sheet, 27.29% random coil, 33.33% α-helix and 17.10% of anti-parallel β-sheet like secondary structure (Figure S7B & B′).

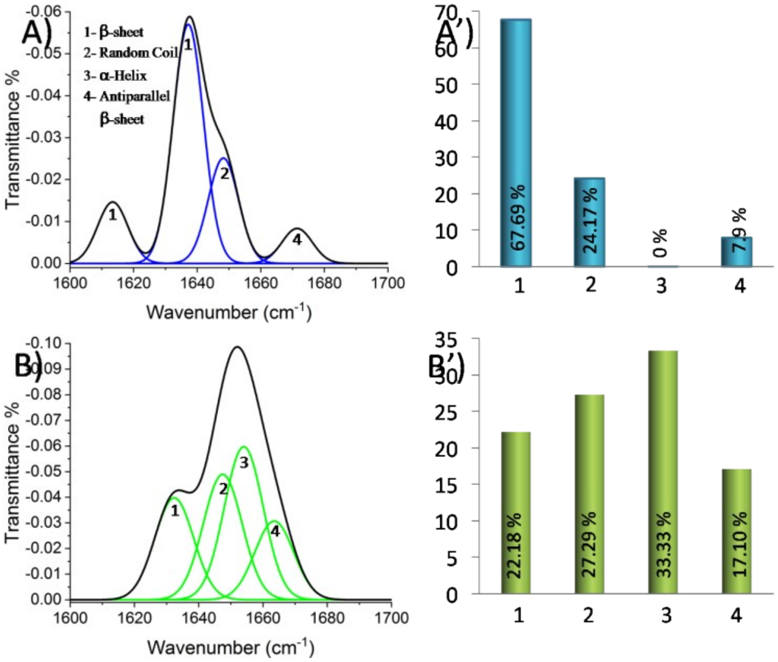

Figure S7. The picture depicts a deconvolution analysis of the amide I region (1600-1700 cm^{-1}). A) FT-IR spectra of 200 μM solution of **sPA1-GNPs** and A‘) corresponding distribution of secondary structural components clearly shows the presence of rich β-sheet structures content along with a small portion of random coil structures. B) representing FT-IR spectrum of **sPA2-GNPs** and B‘) its corresponding secondary structural components representing the emergence of all three, i.e. β-sheet, α-helix, and random coil structures.

11.0 TEM analysis of sPA-GNPs hybrid structures: Transmission electron microscopy (TEM) analysis was used to check the fate of sPA-stabilized GNPs. The TEM analysis showed that mono dispersed distorted multi-shape particles along the fiber axis (Fig. S8A and B) of both sPA1 and sPA2 respectively. The high-resolution TEM images (Fig. S8A &B) of GNPs showed the lattice fringes where *d*, the distance between two lattice fringes, are 2.28 Å and 2.3 Å for **sPA1-GNPs** and **sPA2-GNPs** respectively, typically observed for the crystallinity of face centered cubic structure (fcc) metallic gold GNPs (d= 2.35 Å; JCPDS). The selected area electron diffraction (SAED) pattern illustrates the number of strong Bragg reflections which corresponds to the (111), (200), (220), (222), and (420) confirmed the polycrystalline and *fcc* nature of gold nanoparticles (Fig. S8A'' &B'') and absence of spurious diffractions owing to other crystallographic impurities for both the sPAs respectively.

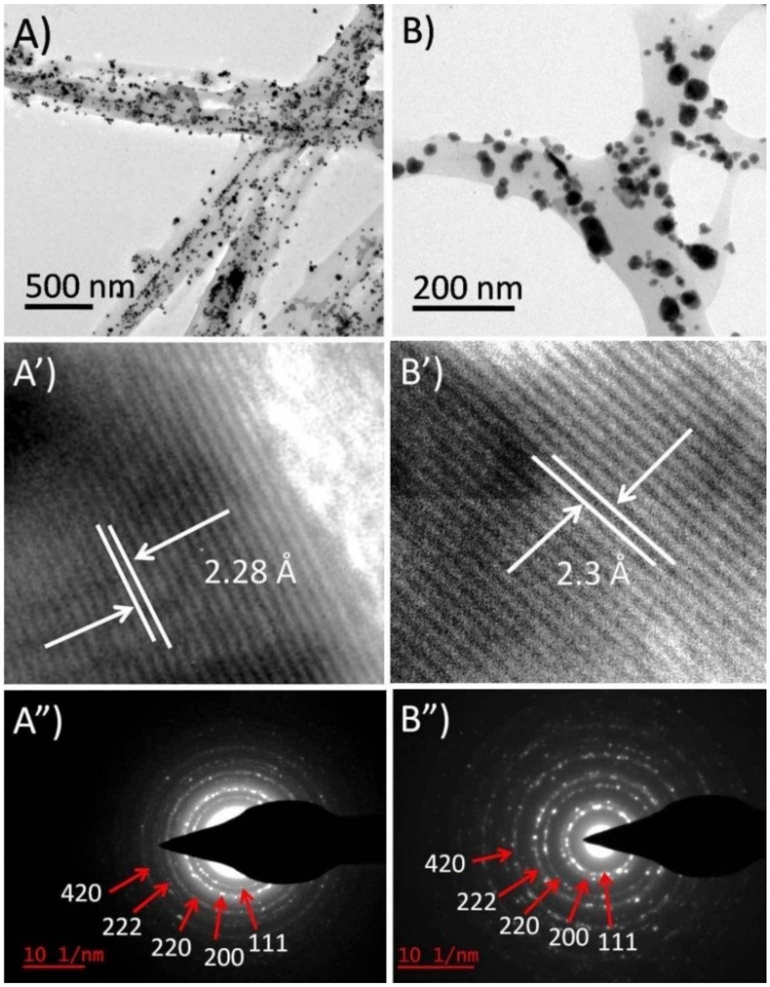

Figure S8. Depicts TEM images of sPA-AuNPs conjugates; A &B) TEM images of fibrous structure of sPA1 and sPA2 decorated by AuNPs., respectively, A' &B') represent corresponding high resolution TEM image of sPA1-AuNPs & sPA2-AunPs that shows the lattice fringes (d= ~2.3 Å &) of AuNPs distinctly A'' &B'') corresponding selected area electron diffraction (SAED) pattern.

12.0 Quantitative Ananlysis of obtained multi-shaped GNPs: Due to the unique optoelectronic properties of gold nanoparticles in various physicochemical environments, they became nanomaterials of special choice for material scientists for nanofabrication purposes. A study of high-resolution magnified TEM images of sPAs-GNPs samples revealed about the presence of various kinds of GNPs geometry (Fig. S9A & Fig. S9B). Therefore a qualitative analysis was done by selecting four different TEM images of **sPA1-GNPs** and **sPA2-GNPs** (Figure S9A & S9B) respectively.

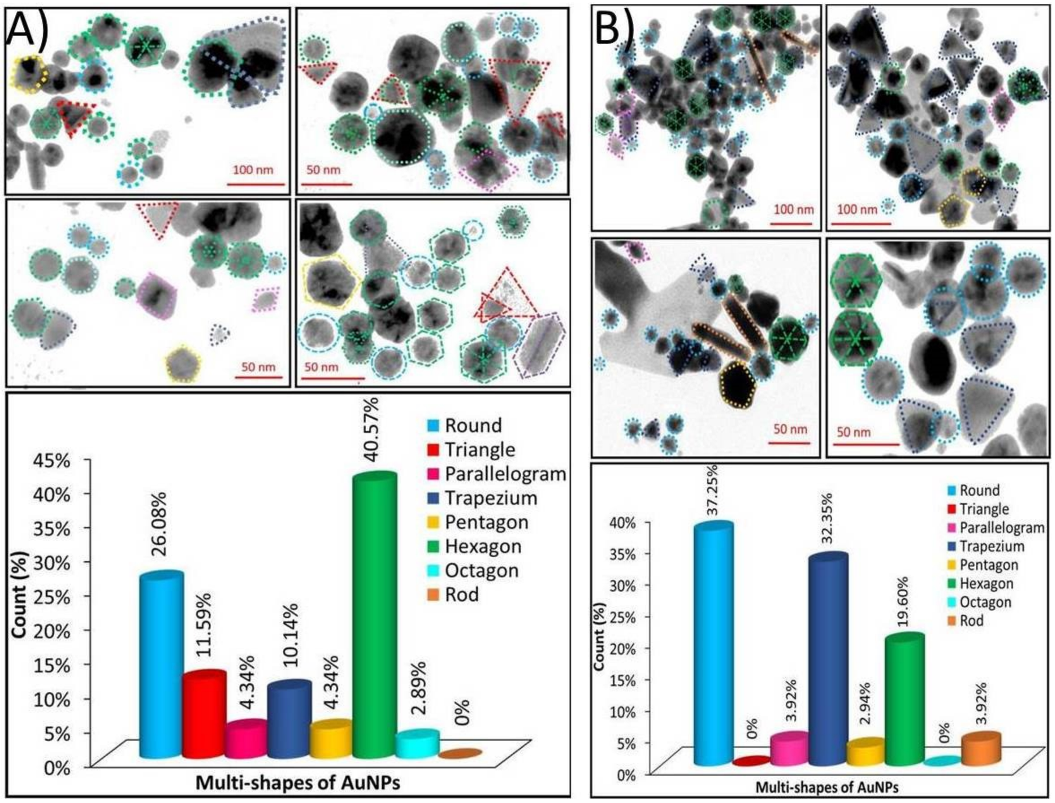

Figure S9. A) *Top:* depicts, a representative TEM image of multi-shaped GNPs synthesized by using **sPA1** showing different kinds of 2D geometries marked by dashed outlines. *Bottom*: is a quantitative analysis of the multi-shapes of AuNPs of the corresponding images. **B)** *Top:* depicts, a representative TEM image of multi-shaped GNPs synthesized by using sPA2 showing different kinds of 2D geometries marked by dashed outlines.Bottom: is a quantitative analysis of the multi-shapes of AuNPs of the corresponding images.

12.0 Power of the sunlight: Our most of the experiments were carried out during the summer season in Dr, Harisingh gour Vishwavidyalaya (A Central University) of Madhya Pradesh, India, therefore the power of sunlight was in the range of 3.0–7.5 kWh/m^2-day (10.8–27 MJ/m^2-day).[1]

1. B. Jamil, A. T. Siddiqui, N. Akhtar *Eng. Sci. Technol. an Int. J.* 2016, ***19***, 1826–1835 (http://dx.doi.org/10.1016/j.jestch.2016.10.004)

Since, we are performing the experiments, mainly synthesis of AuNPs followed by nanowelding of caged smaller gold nanosheets in the presence of ordinary day sunlight radiation which mainly consists of three major components, i.e. i) ultraviolet light, ii) visible light and iii) infrared radiations hence revealed the presence of mixed wavelength ranges fromUV-Vis to infrared.

13.0 A proposed mechanistic model for the formation of nanowelded submicrometer sized gold sheet: To understand the nanowelding process of smaller multishaped gold nanosheets guided by sPA (Fig. S10) a schematic mechanistic model was proposed (Fig. S10). We have taken sPA1 assisted formation of gold microsheets as a representative example. It is now well established that the sPA1 gets self-assembled into micelles followed by robust fibrous assembly. Since the solution of sPA1 has the possibility to contain micelles and long rod-like assembled structures therefore upon addition of Au(III) ion solution these structures are converted to different kinds of supermicellar structures. Such metal ion-mediated supermicellar structures when exposed to sunlight for an appropriate time may lead to gold nanocolloid which contain multi-shaped gold nanosheets (Fig.S10) embedded sPA nanostructures. Such metal-sPA hybrid nanostructures when further exposed to sunlight for a longer duration lead to two-dimensional intact gold microsheets (Fig. 3 & 4 main text). The growth of the larger sheets or microsheet ultimately stops followed by its isolation from sPA envelope (see the red arrow in fig. S10). This perhaps is due to the larger cumulative surface area of the microsheets absorbing more heat and subsequently may produce high thermal energy that leads to dehydration of the enveloped sPA nanostructures. This process resulted in the formation of well defined intact microsheets (Fig.S10, TEM images).

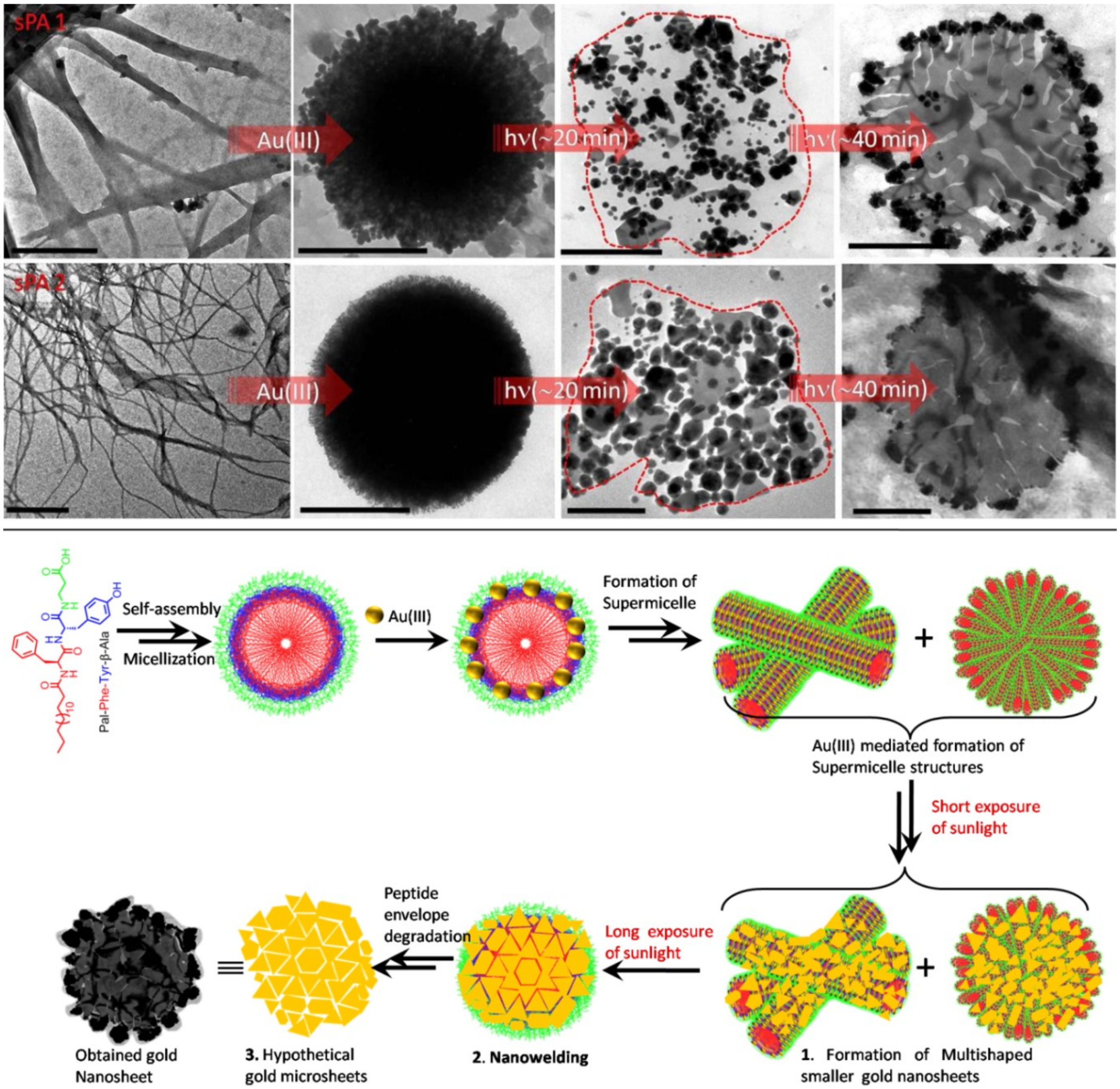

Figure S10. Depicts**,** nanowelding of multi-shaped gold nanosheets. Plasmonic heating-based shape transformation of nanosheets to gold microsheet structures.

14.0 Rising of temperature during the thermoplasmonic welding(Scheme-1): Briefly, photothermal conversion followed by self-limited welding is the two very important sequential steps during thermoplasmonic welding (scheme-1).[1] In the present case when gold nanostructures illuminated by sunlight lead local surface plasmon resonance (LSPR) with a distinct frequency. The squeezing of light into the nanometer range by LSPRs allows the heat at the nanoscale dimension. The metallic nanostructures then dissipate it to nearby NP or reradiate it again into its surrounding by absorption and scattering phenomenon. The heat absorption leads to plasmonic coupling between adjacent particles and concentrates light into highly localized regions that are referred to as hotspots. Such hotspots are present between various nanostructures and are situated in the range of nanoscale gaps. An increase in heat generation between adjacent materials via the existence of hotspots can be realized in a gap region that is higher than that of its other surrounding regions. Therefore, the presence of a hotspot leads to heat distribution over the materials, which is conducive to the subsequent self-limited Welding.